Supporting Information for

Surface oxidized two-dimensional antimonene nanosheets for electrochemical ammonia synthesis under ambient conditions

Munkhjargal Bat-Erdene,[a]† Guangrui Xu,[b,c]† Munkhbayar Batmunkh,[a,d] Abdulaziz S. R. Bati,[a] Jessica J. White,[d] Md J. Nine,[e] Dusan Losic,[e] Yu Chen,[c] Yun Wang,[d] Tianyi Ma,[b] and Joseph G. Shapter*[a]

[a] Australian Institute for Bioengineering and Nanotechnology, The University of Queensland, Brisbane, Queensland 4072, Australia. E-mail: j.shapter@uq.edu.au

[b] Discipline of Chemistry, School of Environmental and Life Sciences, The University of Newcastle (UON), Callaghan, New South Wales 2308, Australia.

[c] Key Laboratory of Macromolecular Science of Shaanxi Province, Key Laboratory of Applied Surface and Colloid Chemistry (Ministry of Education), Shaanxi Key Laboratory for Advanced Energy Devices, School of Materials Science and Engineering, Shaanxi Normal University, Xi'an 710062, PR China.

[d] Centre for Clean Environment and Energy, School of Environment and Science, Griffith University, Gold Coast, Queensland 4222, Australia.

[e] School of Chemical Engineering and Advanced Materials, The University of Adelaide, Adelaide, South Australia 5005, Australia.

† These two authors made an equal contribution to this work.

Experimental Procedures

Materials. Unless otherwise stated, all chemicals were purchased from Sigma-Aldrich Co., Ltd., Australia. Crystalline antimony (Sb) (99.9999% purity) was obtained from Smart Elements.

Exfoliation of bulk Sb. Few-layer antimonene (FL-Sb) nanosheets were prepared in a 4:1 isopropanol/water mixture by exfoliating bulk Sb crystals using a combination of ball milling and ultrasonication. Bulk Sb crystals were put in a zirconia milling pot with isopropanol/water solvent. The samples were then ball milled using Retsch planetary ball mill (PM 200) with zirconia balls (1 mm) at 300 rpm for 30 min. After drying (at 50 ^{o}C for 6-8 h), the ball milled Sb flakes (30 mg) were re-dispersed in 4:1 isopropanol/water mixture (10 mL) for further exfoliation. The exfoliation was carried out in a bath ultrasonication for 40 min. Then the resulting black suspension was centrifuged at 3000 rpm for 3 min and the dark gray supernatant was recovered.

Materials characterization. Atomic force microscopy (AFM) was performed in air using Asylum Research Cypher S with Asylum Research software, operating in standard tapping mode configuration using AIR cantilever holder. The AFM probe used was high accuracy noncontact composite probe with silicon body, polysilicon lever and silicon high resolution tip (tip curvature radius: <10 nm) from TipsNano. Set-point, drive-amplitude, scan rate and gain values were tuned to optimize image quality and flake thickness. The AFM topography images have been flattened and thickness measurements were made using the section analysis tool of Asylum Research software. The samples for AFM analysis were prepared on silicon substrates by spin coating the as-prepared solutions at 2000 rpm for 20 s.

UV-vis absorption of the FL-Sb dispersions was studied using a UV-vis spectroscopy (Shimadzu UV-2600) at wavelength ranging from 200 nm to 800 nm with an interval of 1 nm. Raman spectra were acquired using a WITec alpha300 RA+S Raman microscope at an excitation laser wavelength of 532 nm with a 20x objective. The grating used was 600 grooves mm^{-1}. The excitation laser power levels were kept as low as possible to prevent sample damage.

X-ray photoelectron spectroscopy (XPS) data were acquired using a Kratos Axis ULTRA X-ray Photoelectron Spectrometer incorporating a 165 mm hemispherical electron energy analyzer. The incident radiation was monochromatic Al K_{α} X-rays (1486.6 eV) at 225 W

(15 kV, 15 mA). Survey scans were collected at an analyzer pass energy of 160 eV while high-resolution (HR) scans used a pass energy of 20 eV. Survey scans were carried out at binding energies between 1200 eV and 0 eV with 1.0 eV steps and 100 ms dwell time. HR scans were run with 0.05 eV steps and 250 ms dwell time. Base pressure in the analysis chamber was 1.0×10^{-9} torr and during sample analysis 1.0×10^{-8} torr.

Bright-field transmission electron microscopy (TEM) images were acquired using a FEI Titan Themis. Scanning transmission electron microscopy (STEM) imaging and Energy-Dispersive X-ray (EDX) elemental mapping were carried out also on a FEI Titan Themis S-TEM instrument. The STEM probe was aberration corrected, enabling sub-angstrom spatial resolution, and High Angle Annular Dark Field (HAADF) images were obtained.

Electrochemical measurements. All electrochemical measurements were conducted on a CHI 660D electrochemical workstation with three-electrode or two-electrode system using a saturated calomel electrode and a carbon rod as the reference and counter electrodes, respectively. Nitrogen reduction reaction (NRR) experiments were performed with N_2-saturated or Ar-saturated 0.1 M KOH solutions in a two-compartment cell (80 mL in each cell compartment) under ambient conditions. The H-type cell was separated by a Nafion 117 membrane. Before NRR measurements, the Nafion membrane was protonated by boiling in the following solutions subsequently: DI water (1 h), H_2O_2 (1 h), DI water (1h), 0.5 M H_2SO_4 (3 h), and DI water (6 h). Copper foams (CFs) were washed with 0.01 M HCl and DI water and used as the working electrodes.

The electrocatalyst ink was prepared by mixing as-prepared FL-Sb nanosheets with (5%) Nafion in IPA/DI water (4:1 v/v). The concentration of the FL-Sb dispersion was □ 0.068 g mL^{-1}. Then 150 μL ink was dropped on the CF electrode with an area of 1×1 cm^2. The linear sweep voltammetry (LSV) was scanned at potentials ranging from 0.30 V to –0.70 V with an interval of 0.001 V in N_2-saturated and/or Ar-saturated 0.1 M KOH solutions. Chronoamperometry was used to generate NH_3 during the NRR at different potentials ranging from +0.05 to –0.70 V vs reversible hydrogen electrode (RHE). The electrolyte was purged with N_2 for 30 min prior to the measurements. A pure N_2 was continuously fed into the cathodic compartment using a properly positioned sparger during the experiment.

Determination of ammonia (NH_3). The concentration of NH_3 in the electrolyte was detected by the indophenol blue method.[1] In detail, 10 mL KOH electrolyte was taken from the cathodic chamber and added into a test tube, to which 400 μL of solution containing 0.04 g phenol

dissolved in ethyl alcohol (95%) and $C_5FeN_6Na_2O{\cdot}H_2O$ (0.5 wt%) was successively added. Then 1000 μL oxidizing reagent containing 800 μL of 50 g trisodium citrate ($Na_3C_6H_5O_7$) and 2.5 g sodium hydroxide (NaOH) dissolved in 250 mL DI water and 200 μL sodium hypochlorite (NaClO) was also added into the test tube. After the mixed solution was left in the dark for 3 h at room temperature, an UV-vis spectrophotometer was used to measure the absorption spectrum of the solution. The absorption peak centered at 650 nm, which indicates the formation of the indophenol blue, was used to determine the amount of NH_3. Ammonia chloride (NH_4Cl) solutions with known concentrations were used to calibrate the concentration–absorbance standard curves.

The concentrations of the produced NH_3 were also detected based with an ammonia-sensitive selective electrode. First, the meter measurement mode changed to mV mode, and the electrode soaked in 50 mL 0.1 M KOH solution with 1 mL alkaline reagent for 15 min. Then 50 mL of each standard solutions with 1 mL alkaline reagent was measured under the same conditions. The measurement was recorded after stabilizing the solutions to obtain standard curve (the slope ranging between 54 and 60 in the 20-25 ^oC temperature range is expected). Then, 50 mL electrolyte solution containing 1 mL alkaline reagent was measured under the same conditions.

Determination of the by-product hydrazine (N_2H_4). The N_2H_4 concentration in the electrolyte was determined by the Watt and Chrisp method.[2] 10 mL electrolyte was taken after the electrolysis and mixed with 5 mL colour reagent which was prepared by mixing ethanol (300 ml), concentrated HCl (30 mL), and p-dimethylaminobenzaldehyde (5.99 g). After stirring for 15 min at room temperature, UV–vis measurements were carried out and the absorption peak centered at 455 nm was used to determine the N_2H_4 amount. Standard hydrazine monohydrate solutions with known concentrations were used to plot the calibration curves.

Calculation of the NH_3 yield and Faradaic efficiency. The mass-normalized yield rate of NH_3 was calculated as follows: $v_{NH3} = (c_{NH3} \times V) / (m \times t)$, where c_{NH3} is the concentration of NH_3 in the electrolyte, V is the volume of electrolyte solution, m is the mass of catalyst loading on CF, t is the reduction reaction time, and A is the surface area of the working electrode. The faradaic efficiency (FE) of NH_3 production can be calculated based on the following equation: $FE = (3F \times c_{NH3} \times V / (17 \times Q)) \times 100\%$, where F is the Faraday constant (96485 C mol^{-1}), Q is the total charge passed through the electrodes during the reaction.

Computational details. The density-functional theory (DFT) computations were conducted using the Vienna ab initio simulation package (VASP) based on the projector augmented wave (PAW) method.[3, 4] Electron-ion interactions were described using standard PAW potentials, with valence configurations of $5s^2 5p^3$ for Sb, $2s^2 2p^4$ for O, and $2s^2 2p^3$ for N. A plane-wave basis set was employed to expand the smooth part of wave functions with a cut-off kinetic energy of 520 eV. The exchange and correlation functional parameterized by Perdew-Burke-Ernzerhhof (PBE),[5] a form of the general gradient approximation (GGA), was used throughout. Since the interactions between the N_2 and catalyst were quite weak, the correction of van der Waals force was also considered by using the DFT-D3 method.[6] The monolayer of antimonene was simulated using a supercell model. The Sb_2O_3 (010) surface was modelled using a slab model with 10 atomic layers. The bottom fix layers are fixed at the bulk position and the other atoms are allowed to relax during the structural optimization. The (3×3) and (2×2) surface cells were employed for antimonene and Sb_2O_3, respectively, for the study on the adsorption of N_2 with one N_2 molecule on topmost surface layer. The corresponding k-point grids were (5×5×1) and (3×2×1) for antimonene and Sb_2O_3, respectively. A sufficiently large vacuum region of 15 Å was used for all systems to ensure the periodic images to be well separated. The N_2 molecule was calculated in a 20 × 20 × 20 $Å^3$ box. The convergence criterion for the electronic self-consistent loop was set to 10^{-5} eV. The atomic structures were optimized until the residual forces were below 0.002 eV $Å^{-1}$.

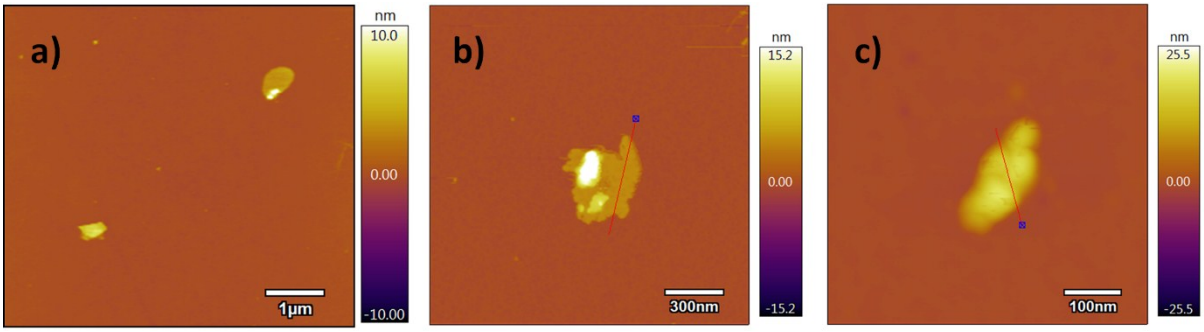

Fig. S1 AFM images of the as-prepared FL-Sb nanosheets on a Si substrate.

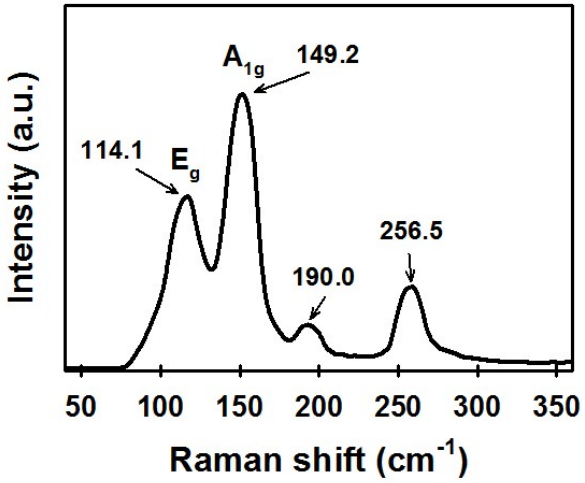

Fig. S2 Raman spectrum of bulk antimony (Sb) crystal.

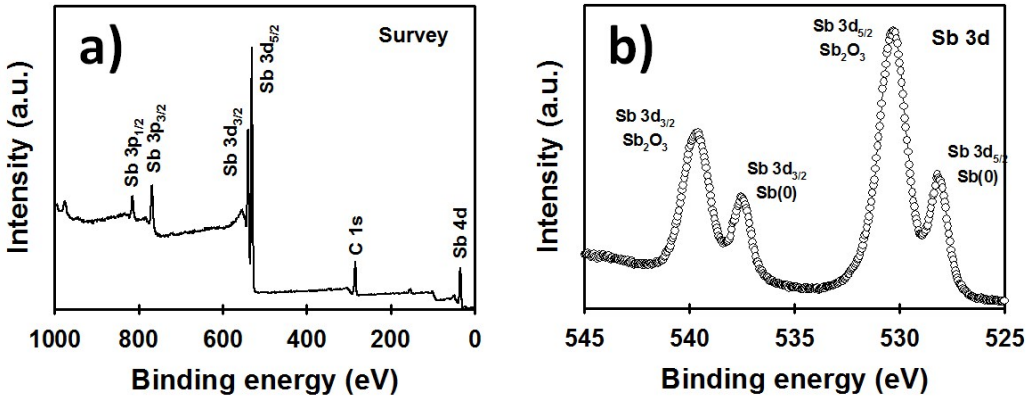

Fig. S3 (a) XPS survey scan and (b) high-resolution XPS Sb 3d spectrum of bulk Sb.

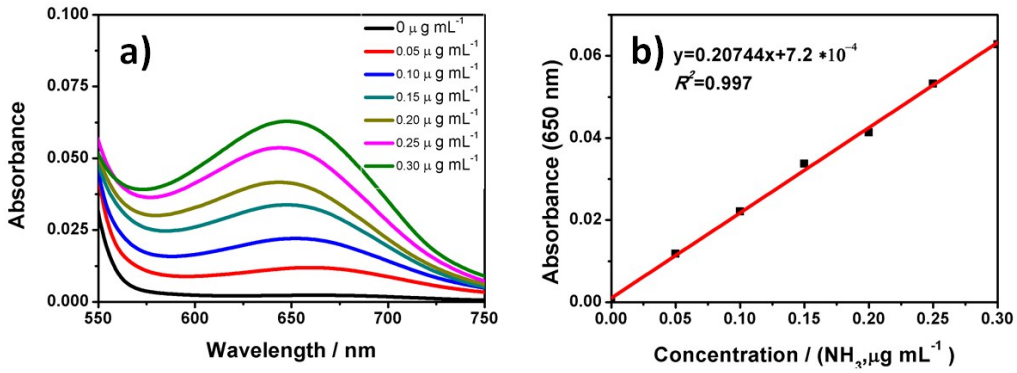

Fig. S4 Determination of the produced NH_3 in 0.1 M KOH. (a) UV-vis absorption spectra and (b) the corresponding calibration curves for the colorimetric NH_3 assay using the indophenol blue method in 0.1 M KOH. The absorbance at 650 nm was used for the calibration, and the fitting curve shows good linear relation of absorbance with NH^{4+} ion.

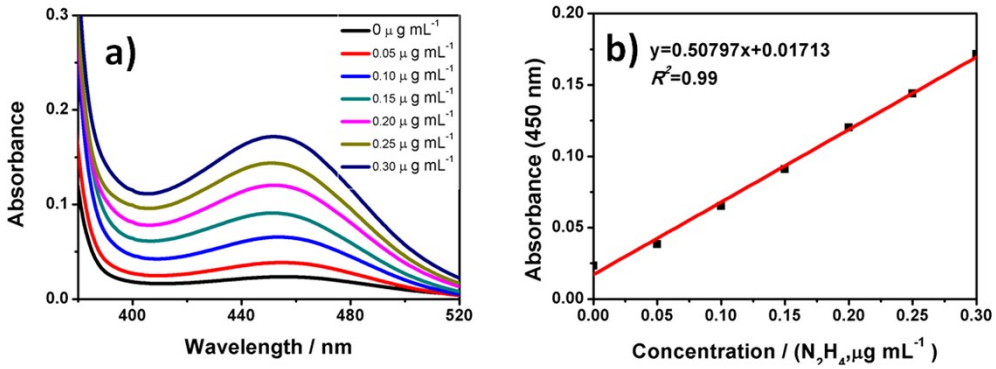

Fig. S5 Determination of the produced $N_2H_4 \cdot H_2O$ in 0.1 M KOH. (a) UV-Vis absorption spectra and (b) the corresponding calibration curves for the colorimetric N_2H_4 assay using the Watt and Chrisp method. The absorbance peak centered at 455 nm was used for calibration.

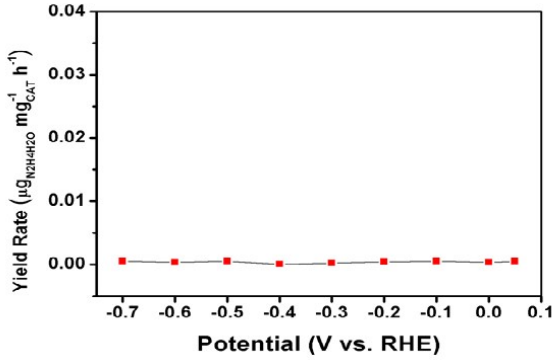

Fig. S6 N_2H_4 yield rate as a function of applied potentials, revealing no by-product N_2H_4 was produced during the catalysis.

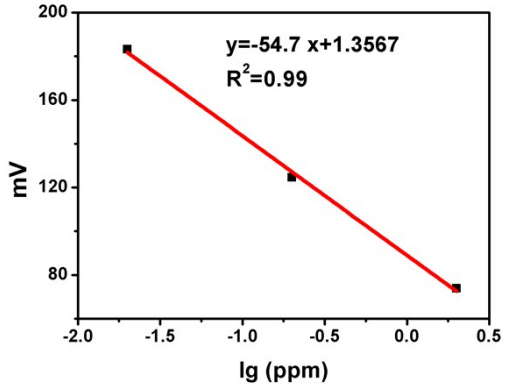

Fig. S7 Calibration curve for the determination of the produced NH_3 in 0.1 M KOH by ammonia-selective electrode method.

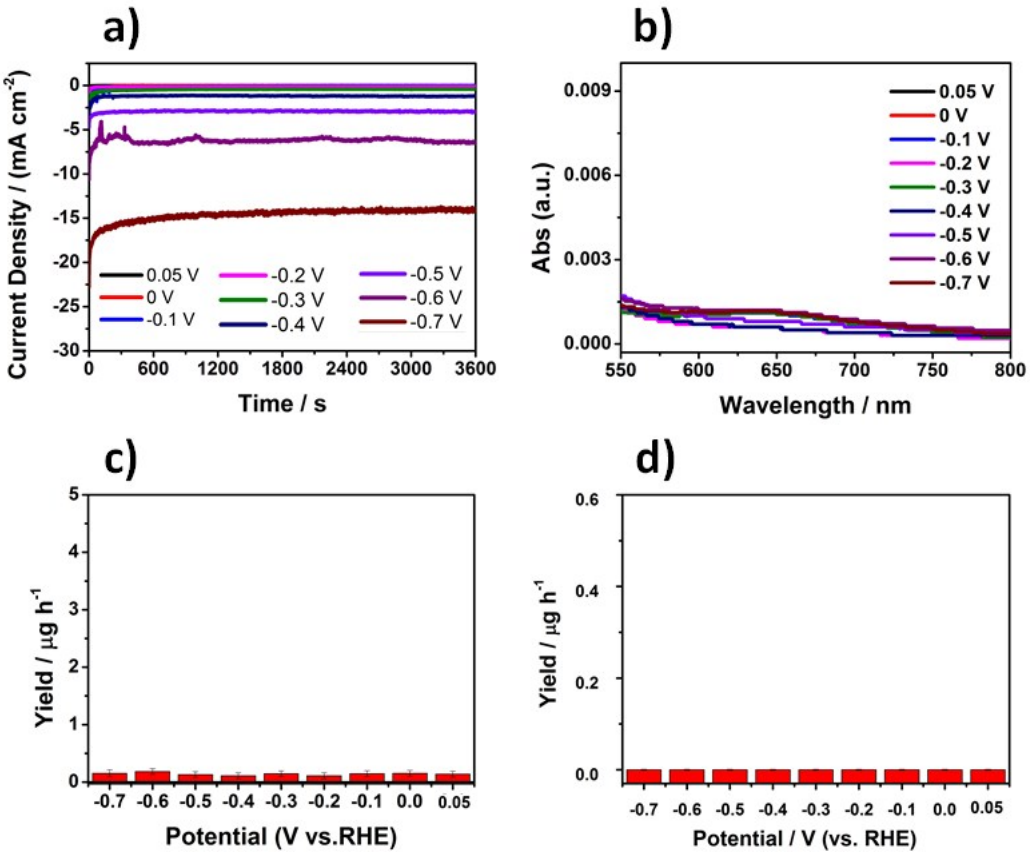

Fig. S8 a) Chronoamperometric curves of the electrode (CF) without catalyst in N_2-saturated 0.1 M KOH electrolyte at different potentials. (b) UV-vis absorption spectra of the KOH electrolyte stained with the indophenol indicator after charging at different potentials for 1 h in the working electrode without catalyst, and (c) the corresponding NH_3 yield for the NRR (indophenol blue method). (d) NH_3 yield rate determined by an ammonia selective electrode.

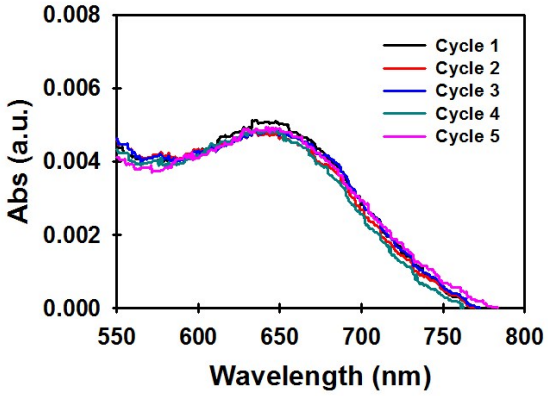

Fig. S9 UV-vis absorption spectra of the KOH electrolyte stained with the indophenol indicator after charging at –0.1 V under five consecutive cycles.

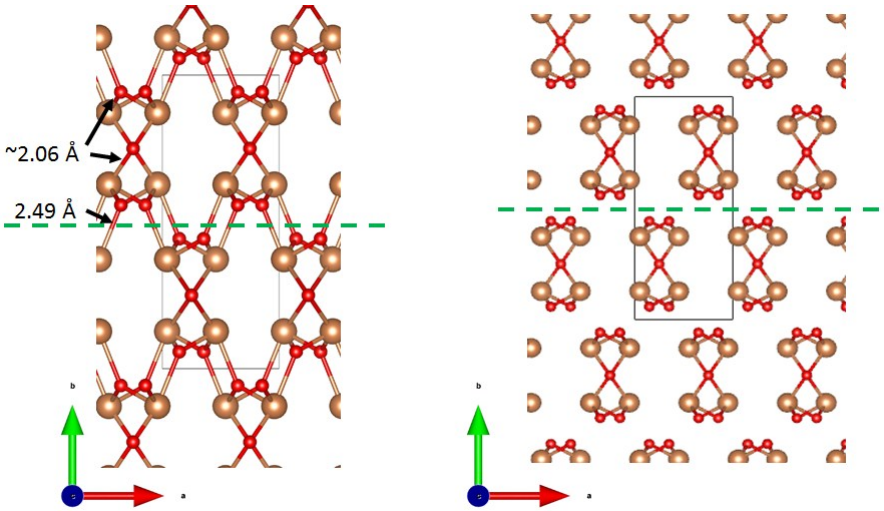

Fig. S10 Structure of Sb_2O_3 bulk crystal. The two structures are identical. The only difference is that the longer Sb-O bonds (2.49 Å) are not shown in the right panel. The longer bond length suggests a weaker interaction between Sb and O atoms. As such, the (010) surface is easier to form by breaking the bonds in the plane indicated by the dashed green line.

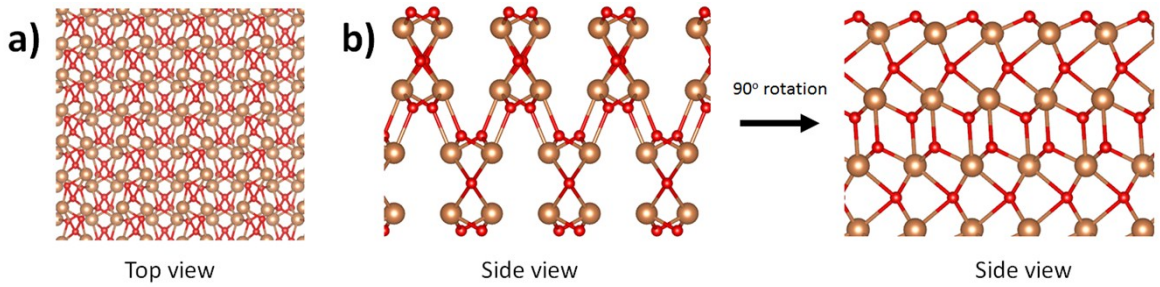

Fig. S11 Structure (top view and side view) of Sb_2O_3 (010) surface considered for the DFT calculation.

Table S1. Summary of NRR performances (NH_3 yield and FE) of different catalysts.

Catalyst	NH_3 yield	FE (%)	Electrolyte	Overpotential (vs. RHE)	Ref
Few-layer antimonene nanosheets (FL-Sb)	133.1 μg h^{-1} mg^{-1}_{CAT}	11.6	0.1 M KOH	0.05 V	This work
Au/TiO_2	21.40 μg h^{-1} mg^{-1}_{CAT}	8.11	0.1 M HCl	–0.20 V	[7]
a-Au/CeO_x–RGO	8.30 μg h^{-1} mg^{-1}_{CAT}	10.10	0.1 M HCl	–0.20 V	[8]
Pd/C	4.50 μg h^{-1} mg^{-1}_{CAT}	8.20	0.1 M PBS	0.10 V	[9]
Ru@NC	3.665 μg h^{-1} mg^{-1}_{CAT}	7.50	0.1 M HCl	–0.21 V	[10]
Ru nanoparticles	0.55 μg h^{-1} cm^{-2}	5.40	0.01 M HCl	0.01 V	[11]
Ru/MoS_2	6.98 μg h^{-1} mg^{-1}_{CAT}	17.60	0.01 M HCl	–0.15 V	[12]
Mo_2N nanorod	78.4 μg h^{-1} mg^{-1}_{CAT}	4.50	0.1 M HCl	–0.30 V	[13]
MoO_2	12.20 μg h^{-1} mg^{-1}_{CAT}	8.20	0.1 M HCl	–0.15 V	[14]
Bismuth nanosheets (BiNSs)	13.23 μg h^{-1} mg^{-1}_{CAT}	10.46	0.1 M Na_2SO_4	–0.80 V	[15]
$BiVO_4$	8.60 μg h^{-1} mg^{-1}_{CAT}	10.04	0.2 M Na_2SO_4	–0.50 V	[16]
Vanadium nitride (VN) nanoparticles	3.30×10^{-10} mol s^{-1} cm^{-2}	6.0	0.05 M H_2SO_4	–0.10 V	[17]
2D Layered W_2N_3	11.66 μg h^{-1} mg^{-1}_{CAT}	11.67	0.1 M KOH	–0.20 V	[18]
MXene	4.72 μg h^{-1} cm^{-2}	4.62	0.5 M Li_2SO_4	–0.10 V	[19]
PEBCD	1.58 μg h^{-1} cm^{-2}	2.85	0.5 M Li_2SO_4	–0.50 V	[20]
Black phosphorus (BP) nanosheets	20.87 μg h^{-1} mg^{-1}_{CAT}	5.07	0.01 M HCl	–0.60 V	[21]
Boron-doped graphene	9.80 μg h^{-1} cm^{-2}	10.80	0.05 M H_2SO_4	–0.50 V	[22]
Polymeric carbon nitride	8.09 μg h^{-1} mg^{-1}_{CAT}	11.59	0.1 M HCl	–0.20 V	[23]
Boron carbide (B_4C)	26.57 μg h^{-1} mg^{-1}_{CAT}	15.95	0.1 M HCl	–0.75 V	[24]

References

1. D. Zhu, L. Zhang, R. E. Ruther and R. J. Hamers, *Nat Mater.*, 2013, **12**, 836.
2. G. W. Watt and J. D. Chrisp, *Anal. Chem.*, 1952, **24**, 2006-2008.
3. G. Kresse and J. Furthmüller, *Comput. Mater. Sci.*, 1996, **6**, 15-50.

4. G. Kresse and D. Joubert, *Phys. Rev. B.*, 1999, **59**, 1758-1775.
5. J. P. Perdew, K. Burke and M. Ernzerhof, *Phys. Rev. Lett.*, 1996, **77**, 3865-3868.
6. S. Grimme, J. Antony, S. Ehrlich and H. Krieg, *J. Chem. Phys.*, 2010, **132**, 154104.
7. M.-M. Shi, D. Bao, B.-R. Wulan, Y.-H. Li, Y.-F. Zhang, J.-M. Yan and Q. Jiang, *Adv. Mater.*, 2017, **29**, 1606550.
8. S.-J. Li, D. Bao, M.-M. Shi, B.-R. Wulan, J.-M. Yan and Q. Jiang, *Adv. Mater.*, 2017, **29**, 1700001.
9. J. Wang, L. Yu, L. Hu, G. Chen, H. Xin and X. Feng, *Nat Commun.*, 2018, **9**, 1795.
10. H. Tao, C. Choi, L.-X. Ding, Z. Jiang, Z. Han, M. Jia, Q. Fan, Y. Gao, H. Wang, A. W. Robertson, S. Hong, Y. Jung, S. Liu and Z. Sun, *Chem*, 2019, **5**, 204-214.
11. D. Wang, L. M. Azofra, M. Harb, L. Cavallo, X. Zhang, B. H. R. Suryanto and D. R. MacFarlane, *ChemSusChem*, 2018, **11**, 3416-3422.
12. B. H. R. Suryanto, D. Wang, L. M. Azofra, M. Harb, L. Cavallo, R. Jalili, D. R. G. Mitchell, M. Chatti and D. R. MacFarlane, *ACS Energy Lett.*, 2019, **4**, 430-435.
13. X. Ren, G. Cui, L. Chen, F. Xie, Q. Wei, Z. Tian and X. Sun, *Chem. Commun.*, 2018, **54**, 8474-8477.
14. G. Zhang, Q. Ji, K. Zhang, Y. Chen, Z. Li, H. Liu, J. Li and J. Qu, *Nano Energy*, 2019, **59**, 10-16.
15. L. Li, C. Tang, B. Xia, H. Jin, Y. Zheng and S.-Z. Qiao, *ACS Catal.*, 2019, **9**, 2902-2908.
16. J.-X. Yao, D. Bao, Q. Zhang, M.-M. Shi, Y. Wang, R. Gao, J.-M. Yan and Q. Jiang, *Small Methods*, 2019, **3**, 1800333.
17. X. Yang, J. Nash, J. Anibal, M. Dunwell, S. Kattel, E. Stavitski, K. Attenkofer, J. G. Chen, Y. Yan and B. Xu, *J. Am. Chem. Soc.*, 2018, **140**, 13387-13391.
18. H. Jin, L. Li, X. Liu, C. Tang, W. Xu, S. Chen, L. Song, Y. Zheng and S.-Z. Qiao, *Adv. Mater.*, 2019, **31**, 1902709.
19. Y. Luo, G.-F. Chen, L. Ding, X. Chen, L.-X. Ding and H. Wang, *Joule*, 2019, **3**, 279-289.
20. G.-F. Chen, X. Cao, S. Wu, X. Zeng, L.-X. Ding, M. Zhu and H. Wang, *J. Am. Chem. Soc.*, 2017, **139**, 9771-9774.
21. L. Zhang, L.-X. Ding, G.-F. Chen, X. Yang and H. Wang, *Angew. Chem. Int. Ed.*, 2019, **58**, 2612-2616.
22. X. Yu, P. Han, Z. Wei, L. Huang, Z. Gu, S. Peng, J. Ma and G. Zheng, *Joule*, 2018, **2**, 1610-1622.
23. C. Lv, Y. Qian, C. Yan, Y. Ding, Y. Liu, G. Chen and G. Yu, *Angew. Chem. Int. Ed.*, 2018, **57**, 10246-10250.
24. W. Qiu, X.-Y. Xie, J. Qiu, W.-H. Fang, R. Liang, X. Ren, X. Ji, G. Cui, A. M. Asiri, G. Cui, B. Tang and X. Sun, *Nat Commun.*, 2018, **9**, 3485.